Accepted Manuscript

N-doped C dot/CoAl-layered double hydroxide/g-C_3N_4 hybrid composites for efficient and selective solar-driven conversion of CO_2 into CH_4

Wan-Kuen Jo, Santosh Kumar, Surendar Tonda

PII: S1359-8368(19)31874-8

DOI: https://doi.org/10.1016/j.compositesb.2019.107212

Article Number: 107212

Reference: JCOMB 107212

To appear in: *Composites Part B*

Received Date: 28 April 2019

Revised Date: 14 July 2019

Accepted Date: 22 July 2019

Please cite this article as: Jo W-K, Kumar S, Tonda S, N-doped C dot/CoAl-layered double hydroxide/g-C_3N_4 hybrid composites for efficient and selective solar-driven conversion of CO_2 into CH_4, *Composites Part B* (2019), doi: https://doi.org/10.1016/j.compositesb.2019.107212.

Graphical abstract

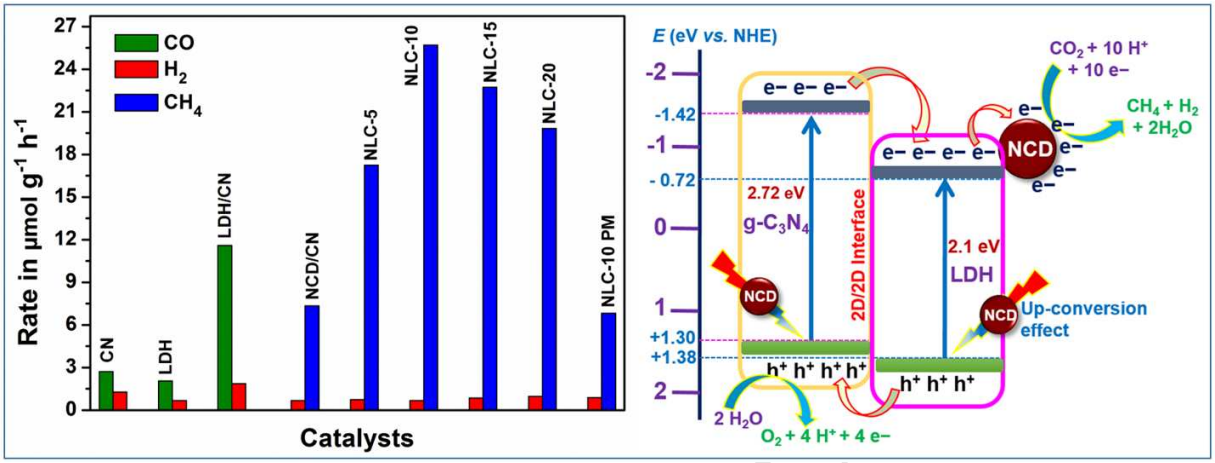

N-doped C dot/CoAl-layered double hydroxide/g-C_3N_4 hybrid composites for efficient and selective solar-driven conversion of CO_2 into CH_4

Wan-Kuen Jo, [a] Santosh Kumar, [b] Surendar Tonda [a,*]

[a] Department of Environmental Engineering, Kyungpook National University, Daegu 702 701, South Korea.

[b] Department of Chemical Engineering, University of Bath, Claverton Down, Bath, BA2 7AY, UK.

*Corresponding Author:
S. Tonda, E-mail: surendar.t86@gmail.com; surendart@knu.ac.kr
Contact No.: +82 53 950 6584.

Abstract

Converting CO_2 into value-added fuel by utilizing abundant solar energy could in principle minimize fossil fuel consumption and anthropogenic CO_2 emissions. However, developing catalytic systems with high selectivity and efficiency is necessary for photocatalytic CO_2 conversion. Here we report the fabrication of a N-doped C dot/CoAl-layered double hydroxide/g-C_3N_4 (NCD/LDH/CN) hybrid heterojunction photocatalyst for high efficiency and selectivity reduction of CO_2 with water into CH_4 under simulated-solar-light illumination. The NCD/LDH/CN hybrid photocatalyst demonstrated remarkable CH_4 production with an optimum rate of 25.69 μmol g^{-1} h^{-1}, an apparent quantum yield of 0.62%, and 99% selectivity for CH_4. This NCD/LDH/CN hybrid system also exhibited exceptional stability and durability during consecutive test cycles with no apparent change in activity. The high activity and stability of the NCD/LDH/CN hybrid toward CO_2 photoreduction is essentially attributable to the strong synergy among the NCD, LDH, and CN constituents, which hinder charge recombination by accelerating charge transportation processes, together with the favorable properties such as broad optical response and good CO_2 adsorption capability. We explored the role of the NCDs in the NCD/LDH/CN hybrid system as a metal-free co-catalyst for the efficient and selective production of CH_4 from CO_2 photoreduction. Thus, the present report provides new insights into the rational fabrication of noble-metal-free photocatalysts for efficient and selective sustainable hydrocarbon production from photocatalytic reduction of CO_2.

Keywords: g-C_3N_4; layered double hydroxide; carbon dots; hybrid heterojunction; solar energy conversion

Introduction

Large-scale consumption of nonrenewable fossil fuels due to increasing industrial growth has led to continually increasing emission of anthropogenic carbon dioxide (CO_2) into our atmosphere. Since CO_2 is a greenhouse gas, this intemperate level of atmospheric CO_2 has caused a series of adverse consequences for the climate system of our planet, including acid rain, rising sea levels, and global warming [1-3]. Despite these disadvantages, CO_2 serves as a C1-feedstock for many chemical industries; therefore, increasing efforts are being devoted to its conversion into energy-rich products [4,5]. Since solar power is a major renewable energy source, solar-powered photocatalytic conversion of CO_2 has been regarded as a potential means of transforming CO_2 into high-energy embedded chemicals or solar fuels (e.g., CO, CH_3OH, C_2H_5OH, CH_4, HCOOH, etc.) that would simultaneously mitigate the global energy crisis and greenhouse effect [6,7]. Nevertheless, the photocatalytic reduction of CO_2 is quite strenuous, due to the high thermodynamic stability of CO_2 molecules and the competing water reduction reaction, which reduce the yield of the desired product [8]. To overcome these limitations and improve the CO_2 reduction efficiency and selectivity, it is essential to develop efficient catalysts capable of harnessing the light absorption across the entire solar spectrum and boosting charge separation and transport.

Since the seminal work by Inoue et al. [9] on photoconversion of CO_2 into value-added chemicals over various semiconductors was published in 1979, numerous heterogeneous photocatalysts have been explored for CO_2 reduction [10]. Recently, the features of two-dimensional (2D) metal-free polymeric graphitic carbon nitride (g-C_3N_4), including high thermal and chemical stabilities, appropriate band gap for visible light absorption, tunable electronic structure, low cost, and nontoxicity, have made it a strong contestant for use in photocatalytic CO_2 reduction reactions [11-13]. Despite these outstanding features, the efficiency of CO_2 reduction is unsatisfactory and hinders the practical application of this

material owing to the limited use of solar energy, low CO_2 adsorption capacity, and low separation efficiency of photoinduced electron–hole pairs. The construction of heterojunction composites by integrating two different semiconductors, particularly into 2D layered architectures with matching conduction band (CB) and valence band (VB) edge potentials, is regarded as an efficient method of improving the separation efficiency of photoexcited charge carriers [14]. Some g-C_3N_4-based 2D/2D composite catalysts reported in the literature have demonstrated considerably enhanced activity for photocatalytic CO_2 reduction performance [15-19].

In addition, the high proximity of CO_2 molecules on the photocatalyst surface is crucial for subsequent CO_2 activation and reduction [20]. Considering their 2D layered architecture and high affinity towards CO_2 molecules, layered double hydroxides (LDHs), as a new class of materials [21-25], are suitable choices for integration with g-C_3N_4. For instance, Hong et al. [26] reported an LDH/g-C_3N_4 composite photocatalyst displaying improved performance for CO_2 reduction to CH_4, which was mainly due to the enrichment of CO_2 molecules on the surface of the composite catalyst. We recently reported a g-C_3N_4/NiAl-LDH hybrid composte for enhanced photoreduction of CO_2 to CO without using a sacrificial reagent [27]. The enhanced activity was mainly attributed to the efficient separation and transfer of photoinduced electron–hole pairs at the heterojunction interfaces. Although these LDH/g-C_3N_4-based composites achieved improved CO_2 adsorption and high charge separation, their relatively poor surface redox chemistry limited the activity and selectivity towards hydrocarbon production.

To overcome these issues, we rationally integrated N-doped C dots (NCDs), CoAl-LDH, and g-C_3N_4 to construct an efficient noble-metal-free NCD/LDH/CN hybrid heterojunction system, which was applied effectively for selective CO_2 reduction to produce CH_4 under simulated-solar-light illumination. The fabricated NCD/LDH/CN hybrids were carefully

characterized using several analytical techniques. Importantly, the NCD/LDH/CN hybrid photocatalyst with appropriate contents of NCDs and LDH showed significantly improved CO_2 photoreduction performance compared to CN, LDH, NCD/CN, and LDH/CN samples. The effects of the LDH content and the multiple roles of the NCDs on the photocatalytic activity of the NCD/LDH/CN hybrid photocatalyst were thoroughly examined. A possible mechanism for the efficient and selective CH_4 production achievable using the present hybrid system was proposed based on the results of photoluminescence (steady-state and time-resolved) and photocurrent experiments. The durability and stability of the hybrid were also probed by conducting consecutive test cycles. To the best of our knowledge, this is the first report of the integration of NCD, LDH, and CN for high efficiency and selectivity reduction of CO_2 into value-added fuels.

Experimental section

Synthesis of photocatalysts

The g-C_3N_4 nanosheets were synthesized by a simple thermal treatment of urea in a muffle furnace. Briefly, 10 g of finely ground urea powder was placed into a covered alumina crucible and then thermally treated to 520 °C for 2 h at a rate of 5 °C/min in a muffle furnace. After cooling to room temperature, the obtained whitish-yellow powder of g-C_3N_4 nanosheets was collected and is herein denoted as CN.

NCDs were prepared from citric acid and urea via a simple hydrothermal route [28]. Typically, 3 g of citric acid and 1 g of urea were dissolved in 30 mL of water and ultrasonicated for 2 h. Then, the solution was transferred into a 50 mL Teflon-lined stainless-steel (TL-SS) autoclave and heated at 180 °C for 5 h. After hydrothermal treatment, the

obtained brown solution was centrifuged at 12,000 rpm for 20 min to remove large particles. Finally, the resultant solution was dried at 80 °C to procure the NCD powder.

The target NCD/LDH/CN hybrid heterojunctions were fabricated via a facile one-pot hydrothermal route, which can be described as follows. Calculated amounts of as-synthesized CN and NCD powders were dispersed through ultrasonication in 160 mL of aqueous solution containing 0.006 M $Co(NO_3)_2.6H_2O$ and 0.002 M $Al(NO_3)_3.9H_2O$. Subsequently, 0.04 M urea and 0.016 M NH_4F were added to the above suspension and magnetically stirred for 2 h. The resultant reaction mixture was transferred into a 200 mL TL-SS autoclave and heated at 120 °C for 24 h. After treatment, the obtained precipitate was collected and washed with water several times, followed by washing with ethanol and drying at 60 °C. NCD/LDH/CN hybrid photocatalysts with the same amount of NCDs (2 wt. %) and different contents of LDH to CN, i.e., 5, 10, 15, and 20 wt. % were fabricated and are denoted herein as NLC-5, NLC-10, NLC-15, and NLC-20, respectively. Pristine LDH was prepared using a similar hydrothermal method, but without the addition of CN and NCDs. For comparison, LDH/CN (10 wt. % of LDH on CN) and NCD/CN (2 wt. % of NCDs on CN) hybrid photocatalysts were also prepared using the same procedure, but in the absence of NCDs and LDH precursors, respectively.

Photocatalytic CO_2 reduction test

Photocatalytic CO_2 reduction experiments were conducted in a homemade stainless steel reactor (80 mL) with a quartz window at the top for passing light irradiation. A 300 W Xe arc lamp was employed as the light source to trigger the CO_2 reduction reaction. In a typical process, 50 mg of the catalyst powder was evenly distributed on a circular glass dish and placed at the bottom of the stainless steel reactor. Then, 300 µL of degassed and CO_2-saturated water (to remove any dissolved O_2) was introduced into the reactor for humidity

and electron donation. Prior to light illumination, the reactor was vacuum-treated and purged with high-purity CO_2 gas for 1 h to ensure that air was completely removed from the reactor. After finishing this process, the reactor was backfilled with CO_2 gas to maintain an inside pressure of about 1 bar. The temperature of the system was held constant at 80 °C to generate water vapor. The pressure and temperature inside the system were continuously monitored by a dial pressure gauge. During the irradiation, 500 μL of gas was periodically extracted from the reactor for quantitative analysis of the products on a Shimadzu Tracera GC-2010 Plus gas chromatograph equipped with barrier ionization detector and He as a carrier gas. The quantification of the production yield was based on a calibration curve of a standard gas mixture.

For the photostability experiment, the catalyst was collected after each photocatalytic run and heated at 120 °C to remove all possible physically adsorbed products. Then, its CO_2 reduction performance was re-evaluated under conditions similar to those mentioned above. The selectivity toward the formation of CH_4 was simply deduced according to the following equation:

$$\mathrm{CH_4\ selectivity\ (\%)} = \frac{8\mathrm{N_{CH_4}}}{8\mathrm{N_{CH_4}} + 2\mathrm{N_{H_2}}} \times 100$$

$$\mathrm{CO\ selectivity\ (\%)} = \frac{2\mathrm{N_{CO}}}{2\mathrm{N_{CO}} + 2\mathrm{N_{H_2}}} \times 100,$$

where N_{CH_4}, N_{CO}, and N_{H_2} are the yields of CH_4, CO, and H_2, respectively.

The apparent quantum yield (AQY) of the photocatalyst was calculated using the following equations:

$$\mathrm{AQY\ (\%)} = \frac{\text{number of reacted electrons}}{\text{number of incident photons}} \times 100$$

$$\mathrm{AQY\ (\%)} = \frac{\text{number of evolved } \mathrm{CH_4} \text{ molecules} \times 8}{\text{number of incident photons}} \times 100.$$

Results and discussion

Characterization of NCDs

The crystal and chemical structures of the NCDs were determined based on the XRD, FTIR, and XPS measurements. The XRD pattern of the NCDs in Fig. 1a displays a broad diffraction peak at 23.8°, which is attributable to the (002) interlayer spacing of a graphitic structure [29]. The FTIR pattern of the NCDs in Fig. 1b reveals the presence of N–H (3000–3400 cm^{-1}), C–H (2650–2900 cm^{-1}), C=O (1767 cm^{-1}), C=N (1658 cm^{-1}), C=C (1551 cm^{-1}), –COOH (1352 cm^{-1}), C–O–C (1237 cm^{-1}), and C–O (1002 cm^{-1}) groups [29-31]. Owing to the existence of these abundant O-containing functional groups, NCDs possess high dispersibility and stability in aqueous solutions. The survey XPS spectrum (Fig. 2a) clearly shows that the NCDs contain C, N, and O. Quantitative XPS analysis revealed 65.7% C, 12.5% N, and 21.8% O, which implies that the synthesized NCDs are C-rich and N-doped. The high-resolution C 1s spectrum (Fig. 2b) can be fitted into four peaks with binding energies (BEs) of 284.5, 286.0, 287.9, and 289.4 eV, corresponding to graphitic-C (C–C/C=C), C–OH, sp^2-bonded C (C=N), and HO–C=O, respectively [28,32]. The N 1s spectrum (Fig. 2c) shows three peaks at 397.4, 399.5, and 401.1 eV for pyridinic-N (C–N–C), graphitic-N ($N-(C)_3$), and amine (N–H) groups [28,33], respectively, implying that the N atoms in the urea were doped into the C dots successfully during the hydrothermal process. The O 1s peaks at 531.0 eV and 533.1 eV shown in Fig. 2d are attributable to oxygen in the form of C=O and C–OH/C–O–C, respectively [33].

The morphological and optical properties of the NCDs were probed by TEM, UV-vis absorption, and PL analyses. Figure 3a displays a TEM image of the synthesized NCDs, revealing that they are well separated from each other without apparent aggregation and possess a quasi-spherical shape. The Gaussian fitting curve (Fig. 3b) demonstrates that the

average size of the NCDs is approximately 2.18 ± 0.25 nm. Although these NCDs are partly composed of amorphous structural groups (e.g., C=C and C−C), the graphitic structure is clearly discernible by high-resolution TEM (HRTEM). The inset of Fig. 3a exhibits lattice planes with a d-spacing of 0.21 nm, which agrees well with the (001) in-plane lattice periodicity of graphitic C [34]. As shown in Fig. 3c, the absorption spectrum of the NCD aqueous solution shows two typical peaks at 236 nm and 334 nm, which can be assigned to the $\pi \rightarrow \pi^*$ transitions of aromatic sp^2 C=C species and $n \rightarrow \pi^*$ transitions that occur in the C=O bonds, respectively [35]. Moreover, the clear brown aqueous NCD solution displays bright blue florescence (inset in Fig. 3c) in the presence of UV light (365 nm). To investigate the optical characteristics of the NCDs further, detailed PL analysis was performed by using different excitation wavelengths (Fig. 3d). As the NCDs were excited by wavelengths at the longer limit (600–900 nm), the up-converted emissions distinctly appear in the shorter wavelength region (400–600 nm), indicating the remarkable up-conversion fluorescent properties of NCDs [28,32]. These PL results indicate that the NCDs might improve the CO_2 reduction efficiency through the conversion of longer wavelength emissions into shorter wavelength light, allowing NCD to be used as a strong energy transfer constituent in the fabrication of hybrid heterojunctions.

Characterization of NCD/LDH/CN hybrids

The crystal structures of the synthesized samples were examined by XRD, and the results are presented in Fig. 4a. For CN, the strong XRD peak at 27.5° can be ascribed to the (002) reflection of a graphite-like stacking of the conjugated aromatic structure with a *d*-value of 0.32 nm, whereas the weak peak at 13.2° corresponds to a typical in-plane structural packing motif of tri-s-triazine ring [36]. The diffraction peaks appearing in the pattern of LDH are well consistent with the standard hydrotalcite-like CoAl-LDH (JCPDS No. 51-0045) with the typical peaks located at 2θ = 11.6° (003), 23.4° (006), 34.5° (012), 39.2° (015), 46.7° (018),

60.2° (110), and 61.5° (018), confirming the successful synthesis of CoAl-LDH [37]. All peaks appearing in the XRD patterns of the LDH/CN and NCD/LDH/CN hybrids are in accordance with those of LDH and CN, implying that LDH was generated on the surface of CN during the hydrothermal process. Moreover, as the amount of LDH increases in the NCD/LDH/CN hybrids, the characteristic peaks of LDH intensify gradually at the expense of the CN peaks (Fig. S1). It is also observable that after adding the NCDs and LDH to CN, the typical peak of CN at 27.5° in the NCD/LDH/CN hybrids is quite shifted from its original position (Fig. S2). These results demonstrate the existence of synergetic interactions among the NCDs, LDH, and CN in the NCD/LDH/CN hybrids. However, no characteristic peaks related to NCDs are detectable in the XRD patterns of the NCD/CN and NCD/LDH/CN hybrids due to the small quantity and relatively low crystallinity of NCDs.

Fig. 4b shows the UV-vis DRS spectra of the synthesized catalysts. CN displays an absorption edge at ~455 nm, reflecting its intrinsic visible-light properties. For LDH, the absorption situated in the UV region (200–300 nm) corresponding to the ligand-to-metal charge transfer within the LDH network, whereas the three bands (450, 490, and 530 nm) located in the visible region can be attributed to d–d transitions of Co (II) species in octahedral coordination geometry [38-40]. Compared to CN, LDH/CN exhibits a slight blue shift along with the mentioned characteristic visible-range absorption bands of LDH, implying the coordination of CN with LDH. In contrast to CN, the NCD/CN hybrid shows an obvious red shift in the absorption edge as well as notably improved optical absorption across the wavelength range investigated, providing solid and direct evidence for the existence of NCDs in the sample. More importantly, analogous enhanced optical responses corresponding to NCDs and the typical visible-range absorption bands related to LDH are observable in all the NCD/LDH/CN hybrids, demonstrating the interactions among NCDs, LDH, and CN in these hybrids. The distinct improvement in the optical response of the NCD/LDH/CN hybrids

can enable efficient utilization of the solar spectrum and therefore promote the production of more charge carriers to improve the efficiency of the photoreduction of CO_2 to produce solar fuels.

In the Tauc plot derived from the UV-vis spectrum (i.e., $(\alpha h\nu)^n$ versus $h\nu$, where h, ν, and α are the Planck constant, light frequency, and absorption coefficient, respectively, and n = 2 for a direct band gap material and n = 1/2 for an indirect band gap material), the bandgap energy of the sample can be estimated based on the horizontal intercept of the extrapolation from the linear region (as depicted in Fig. S2) [41]. Thus, the bandgap energies of CN, LDH, and NLC-10 estimated from Tauc plots are 2.72, 2.1, and 2.62 eV, respectively.

FTIR spectroscopy was utilized to characterize the chemical bonds present in the CN, LDH, and NCD/LDH/CN hybrid heterojunctions, as displayed in Fig. S3. The broad band at 3000–3400 cm^{-1} for CN (Fig. S3a) can be assigned to the stretching vibrations of residual primary and secondary amine groups [19]. Several bands at 1200–1500 cm^{-1} are due to C–N stretching of aromatic rings, and the sharp band at 804 cm^{-1} is the typical peak for tri-s-triazine units [42,43]. No significant changes in these typical bands are observable in the NCD/CN sample compared to CN, implying that there were no notable changes to the basic framework of CN when it was hybridized with the NCDs, which is consistent with previous reports [31,44]. LDH exhibits a strong band at 1354 cm^{-1} corresponding to the bending vibrations of NO_3^- species intercalated in the lamellar network [36]. The absorption band related to the stretching modes of hydroxyl (O−H) groups attached to the brucite layers and stretching vibrations of intercalated water molecules is observable at 3200–3600 cm^{-1} [45]. The bands below 1000 cm^{-1} are characteristic vibrations of M−O, M−OH, and M−O−M (M=Co, Al) in the LDH lattice [27,45,46]. The FTIR spectra of the LDH/CN and NCD/LDH/CN hybrids exhibit all the bands related to CN along with the characteristic band (3200–3600 cm^{-1}) of LDH (Fig. S3b). In addition, the typical band of CN (804 cm^{-1}) is

clearly shifted to a higher frequency region in the FTIR patterns of the NCD/LDH/CN hybrids (Fig. S3c), which might be due to the existence of solid interactions among the NCDs, CN, and LDH in the NCD/LDH/CN hybrids.

The morphological aspects of CN, LDH, and the NCD/LDH/CN hybrids were characterized using SEM and TEM measurements. As appeared in Fig. 5a, CN shows a sheet-like structure with irregular orientation. The TEM image in Fig. 5b further reveals that CN possesses a 2D thin layered structure composed of some mesoporous channels on its surface. LDH possesses a hierarchical flower-like microsphere structure consisting of several self-assembled 2D thin sheets (Figs. 5c and d). The SEM and TEM images (Figs. 5e and f) of NLC-10 clearly indicate that the NCD/LDH/CN hybrid was composed of CN and LDH. Because of their very small size (2.18 nm, as confirmed by the particle size distribution in Fig. 2b), the NCDs are not visible in these SEM and TEM images of NLC-10; however, they can easily be discerned by HRTEM. As expected, the HRTEM image of NLC-10 (Fig. 6a) clearly demonstrates the presence of NCDs, LDH, and CN and their close integration in the NCD/LDH/CN hybrid. Interestingly, the original flower-like microsphere (self-aggregated) morphology of LDH is nowhere to be seen in the SEM or TEM images of NLC-10, but numerous segregated thin LDH sheets are intimately contacted on the CN nanosheet surface. Thus, it can be deduced that during hydrothermal treatment, several LDH sheets tend to grow on the CN surface rather than undergoing self-aggregation, which is due to the opposite surface charges of CN (negative) and LDH (positive). Likewise, owing to the presence of abundant O-containing functional groups (as evidenced by the FTIR and XPS results in Figs. 1b and 2), NCDs also have strong coordination with CN and LDH. Furthermore, clear lattice fringes with *d*-spacings of 0.21, 0.26, and 0.32 nm are observable in the HRTEM image of NLC-10 (Fig. 6b), which correspond to NCDs (100), LDH (012), and CN (002), respectively [27,34,47]. Furthermore, the EDS elemental mapping images of LCR-15 in Figs. 6c–h

indicate the coexistence of C, N, Co, Al, and O, further confirming the close integration of the NCDs, LDH, and CN rather than a mechanical mixture of independent phases in the NCD/LDH/CN hybrid. In addition, the bulk elemental composition of NLC-10 obtained by EDS elemental analysis (Fig. S4) reveals that the atomic ratio of Co:Al in NLC-10 is 2.94, which is very close to the theoretical value for pristine CoAl-LDH, i.e., 3.

XPS analysis was conducted to determine the surface compositions and chemical states of the elements in the CN, LDH, and NLC-10 catalysts accurately. As shown in the survey XPS spectra (Fig. 7a), CN displays peaks related to C and N, whereas LDH reveals the presence of Co, Al, and O. Moreover, the survey XPS profile of NLC-10 displays peaks related to C, N, Co, Al, and O, indicating that the hybrid heterojunction consists of LDH, CN, and NCDs. The high-resolution C 1s spectrum of CN (Fig. 7b) can be fitted into two peaks appearing at 284.5 eV and 288.1 eV, which correspond to adventitious or graphitic C (C–C/C=C) units and N–C=N coordination within the tri-s-triazine ring, respectively [19]. Along with these two peaks, NLC-10 exhibits two additional peaks with BEs of 286.0 eV and 289.5 eV, corresponding to C–OH and HO–C=O of NCDs, respectively [28,32]. Moreover, compared to CN, the intensity of the graphitic C component of NLC-10 is significantly higher, which clearly indicates the presence of NCDs in the hybrid heterojunction. In addition, the N 1s spectrum of CN (Fig. 7c) shows three main peaks at 398.4, 399.8, and 401.0 eV after deconvolution. The two typical peaks at 398.4 eV and 399.8 eV can be assigned to aromatic C–N=C coordination in one tri-s-triazine heteroring and N−$(C)_3$ bridging among three tri-s-triazine moieties, respectively [48]. The weak peak at 401.0 eV corresponds to the amino functional groups (N−H) [36]. Additionally, significant shift in the BEs of the mentioned N components are observable for the NLC-10 hybrid compared to CN, which could be due to the CN and NCD interactions [19]. The O 1s spectra of LDH (Fig. 7d) exhibits three peaks at 530.3, 532.0, and 534.2 eV corresponding to lattice O species (O^{2-}), hydroxide groups (−OH),

and adsorbed water, respectively [49,50]. In addition to these O species, NLC-10 displays extra O components of NCDs at 531.1 eV (C=O) and 533.4 eV (C–OH/C–O–C) [33]. Two peaks at 780.9 eV and 797.2 eV in the high-resolution Co 2p spectrum of LDH (Fig. 7e) can be assigned to Co $2p_{3/2}$ and Co $2p_{1/2}$, respectively [51]. The concomitant two satellite peaks at 786.8 eV and 803.1 eV indicate the high-spin Co^{2+} oxidation state of Co in the LDH. Nevertheless, the BEs of Co $2p_{3/2}$ and Co $2p_{1/2}$ increases for the NLC-10 hybrid heterojunction relative to that of LDH. Meanwhile, the high-resolution Al 2p spectra (Fig. 7f) of both LDH and NLC-10 reveal a typical peak centered at 73.8 eV, which confirms the presence of Al^{+3} species [52]. The significant shift in the BEs of N 1s and Co 2p demonstrate the intimate interfacial interactions among CN, LDH, and the NCDs for rapid charge transfer to boost the CO_2 reduction performance of the NCD/LDH/CN hybrid heterojunction [19,27,51,53].

TGA was performed to analyze the thermal behaviors of CN and LDH, as well as to determine the actual LDH contents in the target NCD/LDH/CN hybrids. The obvious mass-loss region of CN at 550−700 °C is attributable to the combustion of CN (Fig. S5) [43]. The pattern of LDH mainly shows two weight-loss regions, where the first region at 100−200 °C corresponds to the evaporation of physisorbed (surface-adsorbed) and chemisorbed (interlayer) water molecules, and the second region at 200−300 °C is attributable to the elimination of interlayer nitrate ions and dehydroxylation of the brucite-like layers [27,54]. Moreover, no significant weight-loss after 300 °C is observable for LDH, possibly due to the complete transformation of LDH into its respective metal oxides [55]. Analogous mass-loss regions corresponding to LDH and CN were observable for all the NCD/LDH/CN hybrids. In addition, the actual contents of LDH in the NCD/LDH/CN hybrids according to the TGA patterns are 3.2, 8.2, 11.9, and 16.5 wt.% for NLC-5, NLC-10, NLC-15, and NLC-20, respectively.

Photocatalytic CO_2 reduction performance

The photocatalytic CO_2 reduction activities of the fabricated NCD/LDH/CN hybrids were assessed in the presence of water (vapor) under simulated solar-light illumination. For comparison, the CO_2 photoreduction performances of bare CN and LDH samples and binary NCD/LDH and LDH/CN hybrids were also examined under similar experimental conditions. Figure 8a displays the CO_2 photoreduction yields of all the samples after 5 h of light illumination. Because of the suitable band-edge potentials for water reduction reactions, all the fabricated catalysts produced H_2 as a competitive (water) reduction product (Fig. 8b). CN displays minimal CO generation with a total yield of 0.68 μmol, owing to its intrinsic drawbacks, as discussed earlier. Meanwhile, LDH shows relatively low CO_2 photoreduction activity, where the total CO yield is only 0.52 μmol. However, compared to CN, the LDH/CN sample shows enhanced CO production yield, i.e., 2.9 μmol, possibly due to charge transfer between LDH and CN, which can lead to reduced photoinduced charge recombination. Surprisingly, the NCD/CN hybrid produced a different carbonaceous product, CH_4, with a total yield of 1.84 μmol, from CO_2 reduction reaction under the same experimental conditions. Moreover, compared to CN, the NCD/CN hybrid demonstrates significantly enhanced selectivity towards CO_2 reduction against the competitive water reduction reaction, implying that the incorporation of NCDs into the CN framework strongly affects the efficiency and selectivity of CO_2 photoreduction.

Importantly, after incorporating LDH and NCDs into the CN framework, the resulting NCD/LDH/CN hybrids exhibited substantially improved photocatalytic activities for CO_2 reduction to generate CH_4. Among all the NCD/LDH/CN hybrids, the NLC-10 hybrid with 2 wt. % of NCDs and 10 wt. % of LDH displays the highest CH_4 production with a total yield of 6.42 μmol for 5 h, equating to a rate of 25.69 μmol g^{-1} h^{-1} (Fig. 8c), which is manifested as substantial 12.5, 9, 2.2, and 3.5-fold enhancements in productivity compared to those of

LDH, CN, LDH/CN, and NCD/CN, respectively. More remarkably, the amount of H_2 generation was only 0.16 μmol, which means that the selectivity of CH_4 production reached almost 99%. The photocatalytic performance of the NLC-10 hybrid was also compared with those of other catalysts reported in the literature. Notably, the rate of CH_4 production using this optimum catalyst, NLC-10, is several orders of magnitude higher than those of the CN-based and other photocatalytic systems reported previously [26,56-61]. Furthermore, the apparent quantum yield of NLC-10 at 400 nm is 0.62%, which is also far superior to the other state-of-the-art CO_2 photoreduction catalyst systems for CH_4 generation [16,26,31,62,63].

To confirm that the CH_4 generation was not due to organic residues, a control test was performed under an Ar atmosphere. No CH_4 generation was detected for the same NLC-10 hybrid after 5 h of light irradiation. Moreover, no products were detected in the absence of the catalyst, light irradiation, or water, meaning that the CH_4 generation truly originated from the reduction of CO_2 with water vapor in the presence of the NLC-10 hybrid. Similar controlled tests were conducted for all the catalysts before performing the CO_2 reduction experiments. From the photocatalytic activity results, it is also worth noting that, as the amount of LDH in the NCD/LDH/CN hybrids increased beyond its optimum level, i.e., 10 wt. %, a significant decrease in the CH_4 generation was observed. This is because excessive incorporation of LDH into CN led to self-aggregation of LDH (Fig. S6), thereby decreasing the density of LDH/CN heterojunctions, which subsequently resulted in decreased CO_2 photoreduction performance. The CO_2 photoreduction experiments were also conducted for NCD/LDH/CN hybrids synthesized from different amounts of NCDs (i.e., 1, 2, and 3 wt. %) but with the same amount of LDH on CN (10 wt. %) (Fig. S7a). Although the NCD/LDH/CN hybrid with high NCD content (3 wt. %) exhibits improved optical absorption (Fig. S7b), its activity is inferior to that of the optimized catalyst with 2 wt. % of NCDs (NLC-10). This feature might be due to the inner-filter effect of the NCDs via competition for the absorption

of photons with CN and LDH, leading to reduced charge carrier generation and thereby decreasing the CO_2 photoreduction performance [28,64]. These results clearly suggest that suitable contents of LDH and NCDs are important to establish strong synergy among the NCDs, CN, and LDH in the NCD/LDH/CN hybrid for improved CO_2 reduction performance.

To ensure that the synergy among the NCDs, CN, and LDH in the NCD/LDH/CN hybrids is crucial in CH_4 generation, the CO_2 photoreduction activity of NLC-10 was compared with that of a physical mixture of the same weight consisting of NCDs (2 wt. %), LDH (10 wt. %), and CN, denoted here as NLC-10 PM. As shown in Fig. 8, the productivity of the physically mixed NLC-10 PM is much lower than that of NLC-10 hybrid fabricated by the hydrothermal method, and even weaker than binary those of the NCD/CN and LDH/CN hybrids, confirming that strong synergy among the constituents of the NCD/LDH/CN hybrids is necessary for excellent photocatalytic CO_2 reduction activity.

To verify the durability and stability of the NCD/LDH/CN hybrids, the time course of CH_4 generation using the NLC-10 hybrid was obtained under the same test conditions. As displayed in Fig. 9a, the CH_4 generation rate is constant under prolonged light illumination up to 9 h and decreases after 10 h. This CO_2 reduction activity was measured in a closed reactor; therefore, CO_2 exhaustion in the reaction medium may be the primary reason for the decreased CH_4 production [65]. To corroborate the stability of the hybrid, four consecutive test cycles with repeated CO_2 charging in the reactor were conducted. After each test cycle, the catalyst was refreshed and placed in a reactor with fresh aqueous medium. As displayed in Fig. 9b, the amount of CH_4 generation linearly increases in every test cycle, and no significant decline in reaction activity after four successive test cycles is observable. Therefore, the fabricated hybrid maintained excellent stability during the prolonged reaction. The phase and chemical structures of the fresh and recycled catalysts were further analyzed by comparing their XRD and FTIR characteristics (Figs. S8a and 8b). The XRD and FTIR

analysis results reveal no obvious changes in the phase composition and chemical structure of the NLC-10 hybrid after four reaction cycles, further confirming the high structural stability of the hybrid.

Photocatalytic mechanism

The significantly enhanced photocatalytic performance of the NCD/LDH/CN hybrids toward CO_2 photoreduction to CH_4 is essentially attributable to the solid synergy among the constituents along with various favorable properties. As is well known, broad optical response, large surface area, good CO_2 adsorption capability, and high transfer and separation efficiency of photogenerated charge carriers can boost the photocatalytic performance of a catalyst. The UV-vis DRS studies (discussed earlier) demonstrated that incorporating LDH and NCDs on CN distinctly enhances the optical responses of the NCD/LDH/CN hybrids, which can promote the generation of more charge carriers upon light irradiation. This characteristic could be one of the main reasons for the enhanced efficiency of the present hybrid system toward photoreduction of CO_2 to CH_4.

To explain the effect of the surface area on the CO_2 photoreduction activities of the fabricated catalysts, N_2 adsorption–desorption isotherms and corresponding pore-size distribution measurements were performed. All the catalysts in Fig. S9 exhibit type-IV isotherms with H3 hysteresis loops, indicating the presence of a porous structure. The BET surface area (S_{BET}) and Barrett–Joyner–Halenda pore properties of all the catalysts are summarized in Table S1. S_{BET}, the total pore volume, and the average pore diameter of CN are 125.6 m^2/g, 0.324 cm^3/g, and ~58 nm, respectively. The S_{BET} values of all the NCD/LDH/CN hybrids as well as the binary NCD/CN and LDH/CN hybrids are almost the same as or slightly less than that noticed for CN, but their activities are apparently different. Although the surface area of a catalyst is a crucial factor for the improved photocatalytic

activity, it is ruled out as a factor in the present case since it does not significantly influence the CO_2 photoreduction activities of the present NCD/LDH/CN hybrid systems. Instead, the differences among the photocatalytic performances of these catalysts are related to their CO_2 adsorption capabilities, as discussed below.

Figure 10a displays the CO_2 adsorption curves of CN, NCD/CN, LDH/CN, and all the NCD/LDH/CN hybrids. CN shows a decent CO_2 adsorption capacity of 0.26 mmol/g at atmosphere pressure and 298 K temperature. After introducing a small amount (2 wt. %) of NCDs onto the CN surface, the resulting NCD/CN hybrid exhibits an improved CO_2 adsorption capacity of 0.33 mmol/g. This improvement could be due to the existence of amino ($–NH_2$) functional groups on the NCD surface (as evidenced by the XPS results, Fig. 2c), which can increase the CO_2 adsorption ability significantly [34,66]. Meanwhile, the binary LDH/CN hybrid shows an enhanced CO_2 adsorption capacity (0.40 mmol/g) compared to that of CN, probably due to the presence of abundant basic surface hydroxyl (–OH) groups in LDH materials [24,39]. Importantly, the target NCD/LDH/CN hybrids display remarkably enhanced CO_2 adsorption capacities compared to those of CN and the binary NCD/CN and LDH/CN catalysts. These findings clearly demonstrate that the enhanced CO_2 adsorption capability of the NCD/LDH/CN hybrid is another important factor for the excellent photocatalytic CO_2 reduction activity.

To understand how the transfer and separation efficiencies of photogenerated charge carriers effect the photocatalytic performance of the target NCD/LDH/CN hybrid, steady-state and time-resolved PL spectral analysis were performed. Since PL emission results from charge carrier recombination [67,68], the intense PL emission signal observable for CN (Fig. 10b) demonstrates the rapid recombination of charge carriers in it, through band-to-band transitions. The LDH/CN hybrid exhibits notably reduced PL emission intensity compared to that of CN. This difference could be due to efficient interfacial charge separation in the

LDH/CN hybrid arising from well-established 2D/2D heterojunction interfaces, which hampered the charge recombination [27]. Importantly, the NCD/CN catalyst also displays considerable PL quenching relative to that of CN, because NCDs can act as strong electron reservoirs to trap the electrons from CN and can promote the charge transfer process to hinder charge recombination [31]. More importantly, compared to CN and the binary NCD/CN and LDH/CN catalysts, all the NCD/LDH/CN hybrids display drastically decreased PL emission intensities, and the NLC-10 hybrid exhibits the highest PL emission quenching among all the catalysts studied. More importantly, steady-state PL quenching is well-supported with charge carrier lifetimes determined using the biexponential fitting of the PL intensity decay curve (Fig. 10c), according to our previous report [19]. The average charge carrier lifetime (τ) of NCD/LDH/CN is 11.20 ns, which is much higher than those of the bare CN (3.22 ns), NCD/CN (5.15 ns), and LDH/CN (6.60 ns) catalysts (Table S2). This increase probably originated from the joint promotion of charge transfer by LDH and the NCDs at their optimal contents, which efficiently retarded the direct recombination of photoexcited charge carriers. Moreover, the degree of PL emission quenching is in accordance with the CO_2 photoreduction activity results.

To support the excellent charge transfer and separation in the present NCD/LDH/CN hybrid system further, transient photocurrent measurements were conducted for CN, NCD/CN, LDH/CN, and all the NCD/LDH/CN hybrids. Figure 10d compares the transient photocurrent responses of all the catalysts (coated on electrodes) in several on–off cycles of intermittent light illumination. A prompt photocurrent response with good reproducibility is observable for each light turn-on and turn-off event in all the catalysts. Evidently, the photocurrent responses of all the NCD/LDH/CN hybrids are substantially higher than those of CN as well as the binary hybrids. Consistent with photocatalytic activity results, the highest photocurrent response was recorded for the NLC-10 hybrid, indicating that the

incorporation of appropriate amounts of NCDs and LDH can dramatically suppress electron–hole recombination by promoting the interfacial charge-transportation processes, eventually resulting in the outstanding CO_2 photoreduction activity of the NCD/LDH/CN hybrids towards CH_4 production. Therefore, the photocurrent response results together with the PL (steady-state and time-resolved) findings provide sufficient evidence to conclude that the exceptional CO_2 photoreduction activities of the NCD/LDH/CN hybrids mainly resulted from the rapid charge transfer among the NCDs, LDH, and CN, which caused a greater extent of charge separation in the NCD/LDH/CN hybrid system.

In addition, the transfer direction of the photoexcited charge carriers in the present hybrid system depends on the respective band edge potentials of its constituents. In the present study, VB-XPS studies (Fig. S10) were conducted to determine the VB edge potentials of CN and LDH. The VB edge potentials of CN and LDH estimated from the VB-XPS results are +1.30 and +1.38, respectively. Based on the band gap energies of CN (2.72 eV) and LDH (2.1 eV), the CB edge potentials were estimated to be −1.42 eV and −0.72 eV for CN and LDH, respectively. Since the CB potentials of both CN and LDH are more negative than the CO_2/CH_4 reduction potential (E^0), i.e., −0.24 eV versus the normal hydrogen electrode (NHE), the CO_2 reduction reaction to produce CH_4 is theoretically feasible. It can also be seen from VB-XPS results that the VB potential of CN is less positive than that of LDH, while the CB potential of LDH is less negative than that of CN.

Based on the above discussion, a possible mechanism for the remarkable photocatalytic reduction of CO_2 by the NCD/LDH/CN hybrid system was proposed and is presented in Fig. 11. Upon visible light illumination, both LDH and CN can be excited to produce electrons (e^-) in the CB, with the simultaneous production of holes (h^+) in the VB. Due to the intimate 2D/2D heterojunction interface formed between CN and LDH, the generated e^-s from the CB of CN are transferred to the CB of LDH, while the h^+s are transferred in the opposite

direction, preventing direct charge carrier recombination. This process also results in the accumulation of h^+s in the VB of CN and e^-s in the CB of LDH. The accumulated h^+s in the VB of CN further react with H_2O to generate protons (H^+). In the present hybrid system, NCDs play multiple roles in enhancing the CO_2 photoreduction performance. First, owing to their excellent up-converted PL properties (Fig. 2d), NCDs are capable of absorbing longer wavelengths of visible light and then emitting shorter wavelengths. This converted light with shorter wavelength could excite CN and LDH to produce more electrons and holes. Second, due to their excellent electronic conductivities and electron storage capabilities, NCDs could trap the gathered e^-s from the CB of LDH and thereby promote charge separation, as evidenced by the PL and photocurrent analyses discussed above. The e^-s trapped by the NCDs can react with surface-adsorbed CO_2 molecules to produce CO_2 radical anions ($CO_2^{\bullet -}$), which are further converted into CO with the assistance of H^+ [19,62,65]. Liu et al. [69] reported that highly graphitized NCDs with surface N-containing groups exhibited stronger chemical interactions with CO, preventing the desorption of CO molecules on the NCD surface. These strongly adsorbed CO molecules could accept more e^-s followed by H^+ to form intermediates, such as formyl or carbene radicals, and eventually to produce CH_4 [65,69,70]. It was also reported that the competing H_2 generation reaction from water by NCDs is sluggish and kinetically trivial under appropriate test conditions [71,72]. Thus, the self-reaction of H^+ on the NCD surface is less probable than an encounter between H^+ and $CO_2^{\bullet -}$, which could be why the NCD/CN hybrid possessed high selectivity (98%) toward CO_2 reduction reaction against water reduction compared to CN (68%) and LDH/CN (86%).

The reactions that can occur during photoreduction of CO_2 with H_2O to generate solar fuel in terms of E^0 versus NHE are as follows:

$$\mathrm{NCD/LDH/CN} + h\nu \longrightarrow \mathrm{NCD/LDH/CN}\ (h^+_{VB} + e^-_{CB})$$

$$\mathrm{NCD/LDH/CN}\ (h^+_{VB} + e^-_{CB}) \longrightarrow \mathrm{NCD}\ (e^-) + \mathrm{CN}\ (h^+_{VB})$$

$$\mathrm{CN}\ (h^+_{VB}) + 2H_2O \longrightarrow O_2 + 4H^+ + 4e^-;\ E^0 = +0.82\ \mathrm{V}$$

$$\mathrm{CN\ or\ LDH}\ (2e^-) + 2H^+ + CO_2 \longrightarrow \mathrm{CN\ or\ LDH} + CO + H_2O;\ E^0 = -0.53\ \mathrm{V}$$

$$\mathrm{NCD}\ (8e^-) + 8H^+ + CO_2 \longrightarrow \mathrm{NCD} + CH_4 + 2H_2O;\ E^0 = -0.24\ \mathrm{V}$$

$$\mathrm{NCD}\ (2e^-) + 2H^+ \longrightarrow \mathrm{NCD} + H_2;\ E^0 = -0.41\ \mathrm{V}.$$

Conclusions

We successfully fabricated NCD/LDH/CN hybrid heterojunctions via a facile hydrothermal route. The resulting hybrids displayed distinctly improved optical responses and excellent CO_2 adsorption capabilities and, more importantly, dramatically enhanced CO_2 reduction performance to generate CH_4 under simulated-solar-light irradiation. In particular, the optimum NLC-10 hybrid with suitable NCD and LDH contents displayed the highest CH_4 production rate of 25.69 μmol g^{-1} h^{-1} with an AQY of 0.62% and 99% selectivity for CH_4. The significant enhancement in the photocatalytic CO_2 reduction activity of the NCD/LDH/CN hybrids is primarily attributable to the synergistic effect among CN, NCDs, and LDH, which promotes the transfer of photoexcited charge carriers through heterojunction interfaces to suppress electron–hole recombination. Because of their excellent up-converted PL properties, electron storage capacities, and adsorption capabilities, the NCDs in the NCD/LDH/CN hybrids played multiple roles for the efficient and selective production of CH_4 from CO_2 reduction. Due to their high stability and durability in successive CO_2 reduction test cycles, these noble-metal-free NCD/LDH/CN hybrid photocatalysts can be considered potential candidates for practical application in the production of sustainable solar fuels.

Acknowledgments

This work was supported by the National Research Foundation of Korea grant funded by the Korea government (MSIP) (No. 2016R1A2B4009122 and No. 2017R1A4A1015628).

References

[1] Lewis NS, Nocera DG. Powering the planet: Chemical challenges in solar energy utilization. Proc Natl Acad Sci 2006;103:15729–15735.

[2] Sanz-Pérez ES, Murdock CR, Didas SA, Jones CW. Direct capture of CO_2 from ambient air. Chem Rev 2016;116:11840–11876.

[3] Nielsen DU, Hu XM, Daasbjerg K, Skrydstrup T. Chemically and electrochemically catalysed conversion of CO_2 to CO with follow-up utilization to value-added chemicals. Nat Catal 2018;1:244–254.

[4] Kondratenko EV, Mul G, Baltrusaitis J, Larrazabal GO, PerezRamirez J. Status and perspectives of CO_2 conversion into fuels and chemicals by catalytic, photocatalytic and electrocatalytic processes. Energy Environ Sci 2013;6:3112–3135.

[5] Jiao Y, Zheng Y, Chen P, Jaroniec M, Qiao SZ. Molecular Scaffolding Strategy with Synergistic Active Centers To Facilitate Electrocatalytic CO_2 Reduction to Hydrocarbon/ Alcohol. J Am Chem Soc 2017;139:18093–18100.

[6] Yuan YP, Ruan LW, Barber J, Loo SCJ, Xue C. Hetero-nanostructured suspended photocatalysts for solar-to-fuel conversion. Energy Environ Sci 2014;7:3934–3951.

[7] Tu W, Zhou Y, Zou Z. Photocatalytic conversion of CO_2 into renewable hydrocarbon fuels: State-of-the-art accomplishment, challenges, and prospects. Adv Mater 2014;26:4607–4626.

[8] Yang HB, Hung SF, Liu S, Yuan K, Miao S, Zhang L, Huang X, Wang HY, Cai W, Chen R, Gao J, Yang X, Chen W, Huang Y, Chen HM, Li CM, Zhang T, Liu B. Atomically dispersed Ni(I) as the active site for electrochemical CO_2 reduction. Nat Energy 2018;3:140–147.

[9] Inoue T, Fujishima A, Konishi S, Honda K. Photoelectrocatalytic reduction of carbon dioxide in aqueous suspensions of semiconductor powders. Nature 1979;277:637–638.

[10] White JL, Baruch MF, Pander Iii JE, Hu Y, Fortmeyer IC, Park JE, Zhang T, Liao K, Gu J, Yan Y, Shaw TW, Abelev E, Bocarsly AB. Light-driven heterogeneous reduction of carbon dioxide: Photocatalysts and photoelectrodes. Chem Rev 2015;115:12888–12935.

[11] Wang XC, Maeda K, Thomas A, Takanabe K, Xin G, Carlsson JM, Domen K, Antonietti M. A metal-free polymeric photocatalyst for hydrogen production from water under visible light. Nat Mater 2009;8:76–80.

[12] Ong WJ, Tan LL, Ng YH, Yong ST, Chai SP. Graphitic carbon nitride (g-C_3N_4)-based photocatalysts for artificial photosynthesis and environmental remediation: Are we a step closer to achieving sustainability? Chem Rev 2016;116:7159–7329.

[13] Huang P, Huang J, Pantovich SA, Carl AD, Fenton TG, Caputo CA, Grimm RL, Frenkel AI, Li G. Selective CO_2 reduction catalyzed by single cobalt sites on carbon nitride under visible-light Irradiation. J Am Chem Soc 2018;140:16042–16047.

[14] Low J, Cao S, Yu J, Wageh S. Two-dimensional layered composite photocatalysts. Chem Commun 2014;50:10768–10777.

[15] Li M, Zhang L, Fan X, Zhou Y, Wu M, Shi J. Highly selective CO_2 photoreduction to CO over g-C_3N_4/Bi_2WO_6 composites under visible light . J Mater Chem A 2015;3:5189–5196.

[16] Ong WJ, Tan LL, Chai SP, Yong ST, Mohamed AR. Surface charge modification *via* protonation of graphitic carbon nitride (g-C_3N_4) for electrostatic self-assembly construction of 2D/2D reduced graphene oxide (rGO)/g-C_3N_4 nanostructures toward enhanced photocatalytic reduction of carbon dioxide to methane. Nano Energy 2015;13:757–770.

[17] Bafaqeer A, Tahir M, Amin NAS. Well-designed ZnV_2O_6/g-C_3N_4 2D/2D nanosheets heterojunction with faster charges separation via pCN as mediator towards enhanced photocatalytic reduction of CO_2 to fuels. Appl Catal B Environ 2019;242:312–326.

[18] Wang M, Shen M, Zhang L, Tian J, Jin X, Zhou Y, Shi J. 2D-2D MnO_2/g-C_3N_4 heterojunction photocatalyst: *In-situ* synthesis and enhanced CO_2 reduction activity. Carbon 2017;120:23–31.

[19] Jo WK, Kumar S, Eslava S, Tonda S. Construction of Bi_2WO_6/RGO/g-C_3N_4 2D/2D/2D hybrid Z-scheme heterojunctions with large interfacial contact area for efficient charge separation and high-performance photoreduction of CO_2 and H_2O into solar fuels. Appl Catal B Environ 2018;239:586–598.

[20] Chang X, Wang T, Gong J. CO_2 photo-reduction: insights into CO_2 activation and reaction on surfaces of photocatalysts. Energy Environ Sci 2016;9:2177–2196.

[21] Long X, Wang Z, Xiao S, An Y, Yang S. Transition metal based layered double hydroxides tailored for energy conversion and storage. Mater Today 2016;19:213–226.

[22] Zhao Y, Jia X, Waterhouse GIN, Wu LZ, Tung CH, O 'Hare D, Zhang T. Layered double hydroxide nanostructured photocatalysts for renewable energy production. Adv Energy Mater 2016;6:1501974.

[23] Wang Q, O 'Hare D. Recent advances in the synthesis and application of layered double hydroxide (LDH) nanosheets. Chem Rev 2012;112:4124–4155.

[24] Teramura K, Iguchi S, Mizuno Y, Shishido T, Tanaka T. Photocatalytic conversion of CO_2 in water over layered double hydroxides. Angew Chem Int Ed 2012;51:8008–8011.

[25] Ahmed N, Shibata Y, Taniguchi T, Izumi Y. Photocatalytic conversion of carbon dioxide into methanol using zinc–copper–M(III) (M = aluminum, gallium) layered double hydroxides. J Catal 2011;279:123–135.

[26] Hong J, Zhang W, Wang Y, Zhou T, Xu R. Photocatalytic reduction of carbon dioxide over self-assembled carbon nitride and layered double hydroxide: The role of carbon dioxide enrichment. ChemCatChem 2014;6:2315–2321.

[27] Tonda S, Kumar S, Bhardwaj M, Yadav P, Ogale SB. g-C_3N_4/NiAl-LDH 2D/2D hybrid heterojunction for high-performance photocatalytic reduction of CO_2 into renewable fuels. ACS Appl Mater Interfaces 2018;10:2667–2678.

[28] Wang F, Chen P, Feng Y, Xie Z, Liu Y, Su Y, Zhang Q, Wang Y, Yao K, Lv W, Liu G. Facile synthesis of N-doped carbon dots/g-C_3N_4 photocatalyst with enhanced visible-light photocatalytic activity for the degradation of indomethacin. Appl Catal B Environ 2017;207:103–113.

[29] Dong X, Su Y, Geng H, Li Z, Yang C, Li X, Zhang Y. Fast one-step synthesis of N-doped carbon dots by pyrolyzing ethanolamine. J Mater Chem C 2014;2:7477–7481.

[30] Teng X, Ma C, Ge C, Yan M, Yang J, Zhang Y, Morais PC, Bi H. Green synthesis of nitrogen-doped carbon dots from konjac flour with “off–on” fluorescence by Fe^{3+} and L-lysine for bioimaging. J Mater Chem B 2014;2:4631–4639.

[31] Ong WJ, Putri LK, Tan YC, Tan LL, Li N, Ng YH, Wen X, Chai SP. Unravelling charge carrier dynamics in protonated g-C_3N_4 interfaced with carbon nanodots as co-catalysts toward enhanced photocatalytic CO_2 reduction: A combined experimental and first-principles DFT study. Nano Res 2017;10:1673–1696.

[32] Zhang H, Zhao L, Geng F, Guo LH, Wan B, Yang Y. Carbon dots decorated graphitic carbon nitride as an efficient metal-free photocatalyst for phenol degradation. Appl Catal B Environ 2016;180:656–662.

[33] Yang Z, Xu M, Liu Y, He F, Gao F, Su Y, Wei H, Zhang Y. Nitrogen-doped, carbon-rich, highly photoluminescent carbon dots from ammonium citrate. Nanoscale 2014;6:1890–1895.

[34] Chen Z, Mou K, Wang X, Liu L. Nitrogen-doped graphene quantum dots enhance the activity of Bi_2O_3 nanosheets for electrochemical reduction of CO_2 in a wide negative potential region. Angew Chem Int Ed 2018;57:12790–12794.

[35] Suzuki K, Malfatti L, Takahashi M, Carboni D, Messina F, Tokudome Y, Takemoto M, Innocenzi P. Design of carbon dots photoluminescence through organo-functional silane grafting for solid-state emitting devices. Sci Rep 2017;7:5469.

[36] Tonda S, Jo WK. Plasmonic Ag nanoparticles decorated NiAl-layered double hydroxide/graphitic carbon nitride nanocomposites for efficient visible-light-driven photocatalytic removal of aqueous organic pollutants. Catal Today 2018;315:213–222.

[37] Wang Y, Dou L, Zhang H. Nanosheet array-like palladium-catalysts Pd_x/rGO@CoAl-LDH via lattice atomic-confined in situ reduction for highly efficient heck coupling reaction. ACS Appl Mater Interfaces 2017;9:38784–38795.

[38] Rudolf C, Dragoi B, Ungureanu A, Chirieac A, Royer S, Nastro A, Dumitriu E. NiAl and CoAl materials derived from takovite-like LDHs and related structures as efficient chemoselective hydrogenation catalysts. Catal Sci Technol 2014;4:179−189.

[39] Wang K, Zhang L, Su Y, Shao D, Zeng S, Wang W. Photoreduction of carbon dioxide of atmospheric concentration to methane with water over CoAl-layered double hydroxide nanosheets. J Mater Chem A 2018;6:8366–8373.

[40] Poul L, Jouini N, Fievet F. Layered hydroxide metal acetates (metal = zinc, cobalt, and nickel): Elaboration via hydrolysis in polyol medium and comparative study. Chem Mater 2000;12:3123–3132.

[41] Liu J, Liu Y, Liu N, Han Y, Zhang X, Huang H, Lifshitz Y, Lee ST, Zhong J, Kang Z. Metal-free efficient photocatalyst for stable visible water splitting via a two-electron pathway. Science 2015;347:970−974.

[42] Tonda S, Kumar S, Kandula S, Shanker V. Fe-doped and -mediated graphitic carbon nitride nanosheets for enhanced photocatalytic performance under natural sunlight. J Mater Chem A 2014;2:6772–6780.

[43] Kumar S, Tonda S, Baruah A, Shanker V. Synthesis of a novel and stable g-C_3N_4–Ag_3PO_4 hybrid nanocomposite photocatalyst and study of the photocatalytic activity under visible light irradiation. J Mater Chem A 2013;1:5333–5340.

[44] Liu Q, Chen T, Guo Y, Zhang Z, Fang X. Ultrathin g-C_3N_4 nanosheets coupled with carbon nanodots as 2D/0D composites for efficient photocatalytic H_2 evolution. Appl Catal B Environ 2016;193:248–258.

[45] Huang Z, Wang S, Wang J, Yu Y, Wen J, Li R. Exfoliation-restacking synthesis of coal-layered double hydroxide nanosheets/reduced graphene oxide composite for high performance supercapacitors. Electrochim Acta 2015;152:117–125.

[46] Fang J, Li M, Li Q, Zhang W, Shou Q, Liu F, Zhang X, Cheng J. Microwave-assisted synthesis of CoAl-layered double hydroxide/graphene oxide composite and its application in supercapacitors. Electrochim Acta 2012;85:248–255.

[47] Wang Y, Dou L, Zhang H. Nanosheet array-like palladium-catalysts Pd_x/rGO@CoAl-LDH via lattice atomic-confined in situ reduction for highly efficient heck coupling reaction. ACS Appl Mater Interfaces 2017;9:38784–38795.

[48] Feng J, Zhang D, Zhou H, Pi M, Wang X, Chen S. Coupling P nanostructures with P-doped g-C_3N_4 as efficient visible light photocatalysts for H_2 evolution and RhB degradation. ACS Sustainable Chem Eng 2018;6:6342−6349.

[49] Sahoo DP, Patnaik S, Rath D, Parida KM. Synergistic effects of plasmon induced Ag@Ag_3VO_4/ZnCr LDH ternary heterostructures towards visible light responsive O_2 evolution and phenol oxidation reactions. Inorg Chem Front 2018;5:879–896

[50] Chowdhury PR, Bhattacharyya KG. Synthesis and characterization of Co/Ti layered double hydroxide and its application as a photocatalyst for degradation of aqueous Congo Red. RSC Adv 2015;5:92189–92206.

[51] Kumar S, Isaacs MA, Trofimovaite R, Parlett CMA, Douthwaite RE, Coulson B, Cockett MCR, Wilson K, Lee AF. P25@CoAl layered double hydroxide heterojunction nanocomposites for CO_2 photocatalytic reduction. Appl Catal B Environ 2017;209:394–404.

[52] Liang T, Xuan H, Xu Y, Gao J, Han X, Yang J, Han P, Wang D, Du Y. Rational assembly of CoAl-layered double hydroxide on reduced graphene oxide with enhanced electrochemical performance for energy storage. ChemElectroChem 2018;5:2424–2434.

[53] Dou Y, Zhang S, Pan T, Xu S, Zhou A, Pu M, Yan H, Han J, Wei M, Evans DG, Duan X. TiO_2@layered double hydroxide core–shell nanospheres with largely enhanced photocatalytic activity toward O_2 generation. Adv Funct Mater 2015;25:2243–2249.

[54] Zhang Y, Du D, Li X, Sun H, Li L, Bai P, Xing W, Xue Q, Yan Z. Electrostatic self-assembly of sandwich-like CoAl-LDH/polypyrrole/graphene nanocomposites with enhanced capacitive performance. ACS Appl Mater Interfaces 2017;9:31699−31709.

[55] Woo MA, Song MS, Kim TW, Kim IY, Ju JY, Lee YS, Kim SJ, Choy JH, Hwang SJ. Mixed valence Zn–Co-layered double hydroxides and their exfoliated nanosheets with electrode functionality. J Mater Chem 2011;21:4286–4292.

[56] Ong WJ, Putri LK, Tan LL, Chai SP, Yong ST. Heterostructured AgX/g-C_3N_4 (X = Cl and Br) nanocomposites via a sonication-assisted deposition-precipitation approach: Emerging role of halide ions in the synergistic photocatalytic reduction of carbon dioxide. Appl Catal B Environ 2016;180:530–543.

[57] Shi H, Chen G, Zhang C, Zou Z. Polymeric g-C_3N_4 coupled with $NaNbO_3$ nanowires toward enhanced photocatalytic reduction of CO_2 into renewable fuel. ACS Catal 2014;4:3637–3643.

[58] Ong WJ, Tan LL, Chai SP, Yong ST. Heterojunction engineering of graphitic carbon nitride (g-C_3N_4) *via* Pt loading with improved daylight-induced photocatalytic reduction of carbon dioxide to methane. Dalton Trans 2015;44:1249–1257.

[59] Zhang X, Wang L, Du Q, Wang Z, Ma S, Yu M. Photocatalytic CO_2 reduction over B_4C/C_3N_4 with internal electric field under visible light irradiation. J Colloid Interface Sci 2016;464:89–95.

[60] Yu J, Low J, Xiao W, Zhou P, Jaroniec M. Enhanced photocatalytic CO_2-reduction activity of anatase TiO_2 by coexposed {001} and {101} facets. J Am Chem Soc 2014;136:8839−8842.

[61] Yu J, Jin J, Cheng B, Jaroniec M. A noble metal-free reduced graphene oxide–CdS nanorod composite for the enhanced visible-light photocatalytic reduction of CO_2 to solar fuel. J Mater Chem A 2014;2:3407−3416.

[62] Ong WJ, Tan LL, Chai SP, Yong ST, Mohamed AR. Self-assembly of nitrogen-doped TiO_2 with exposed {001} facets on a graphene scaffold as photo-active hybrid nanostructures for reduction of carbon dioxide to methane. Nano Res 2014;7:1528–1547.

[63] Meng X, Ouyang S, Kako T, Li P, Yu Q, Wang T, Ye J. Photocatalytic CO_2 conversion over alkali modified TiO_2 without loading noble metal cocatalyst. Chem Commun 2014;50:11517–11519.

[64] Pan J, Sheng Y, Zhang J, Wei J, Huang P, Zhang X, Feng B. Preparation of carbon quantum dots/TiO_2 nanotubes composites and their visible light catalytic applications. J Mater Chem A 2014;2:18082–18086.

[65] Bae KL, Kim J, Lim CK, Nam KM, Song H. Colloidal zinc oxide-copper (I) oxide nanocatalysts for selective aqueous photocatalytic carbon dioxide conversion into methane. Nat Commun 2017;8:1156.

[66] Sim K, Lee N, Kim J, Cho EB, Gunathilake C, Jaroniec M. CO_2 adsorption on amine-functionalized periodic mesoporous benzenesilicas. ACS Appl Mater Interfaces 2015;7:6792–6802.

[67] Jo WK, Kumar S, Yadav P, Tonda S. In situ phase transformation synthesis of unique Janus Ag_2O/Ag_2CO_3 heterojunction photocatalyst with improved photocatalytic properties. Appl Surf Sci 2018;445:555–562.

[68] Jo WK, Kim YG, Tonda S. Hierarchical flower-like NiAl-layered double hydroxide microspheres encapsulated with black Cu-doped TiO_2 nanoparticles: Highly efficient visible-light-driven composite photocatalysts for environmental remediation. J Hazard Mater 2018;357:19–29.

[69] Liu Z, Wang Z, Qing S, Xue N, Jia S, Zhang L, Li L, Li N, Shi L, Chen J. Improving methane selectivity of photo-induced CO_2 reduction on carbon dots through modification of nitrogen-containing groups and graphitization. Appl Catal B Environ 2018;232:86–92.

[70] Guo S, Zhang H, Chen Y, Liu Z, Yu B, Zhao Y, Yang Z, Han B, Liu Z. Visible-light-driven photoreduction of CO_2 to CH_4 over N,O,P-containing covalent organic polymer submicrospheres. ACS Catal 2018;8:4576−4581.

[71] Wang H, Min S, Wang Q, Li D, Casillas G, Ma C, Li Y, Liu Z, Li LJ, Yuan J, Antonietti M, Wu T. Nitrogen-doped nanoporous carbon membranes with Co/CoP Janus-type nanocrystals as hydrogen evolution electrode in both acidic and alkaline environments. ACS Nano 2017;11:4358−4364.

[72] Wang H, Jia J, Song P, Wang Q, Li D, Min S, Qian C, Wang L, Li YF, Ma C, Wu T, Yuan J, Antonietti M, Ozin GA. Efficient electrocatalytic reduction of CO_2 by nitrogen-doped nanoporous carbon/carbon nanotube membranes: A step towards the electrochemical CO_2 refinery. Angew Chem Int Ed 2017;56:7847–7852.

Figure captions

Fig. 1. (a) XRD and (b) FTIR patterns of the fabricated NCDs.

Fig. 2. XPS spectra of the NCDs. (a) Survey spectrum, (b) C 1s, (c) N 1s, and (d) O 1s.

Fig. 3. (a) TEM image of the NCDs (inset is the HRTEM image) and (b) the corresponding particle size distribution histogram. (c) UV–vis absorption spectrum and (d) up-converted PL spectra of the NCDs.

Fig. 4. (a) XRD and (b) DRS patterns of the prepared LDH, CN, NCD/CN, LDH/CN and NCD/LDH/CN hybrid samples.

Fig. 5. (a, c, e) SEM and (b, d, f) TEM images of CN, LDH, and the NLC-10 catalysts, respectively.

Fig. 6. High-resolution TEM images (a, b) of the NLC-10 hybrid photocatalyst. (c to h) EDS elemental mappings of constituent elements in the NLC-10 hybrid.

Fig. 7. XPS spectra of CN, LDH, and NLC-10 samples. (a) Survey spectra, (b) C 1s, (c) N 1s, (d) O 1s, (e) Co 2p, and (f) Al 2p.

Fig. 8. Time-dependent (a) CO & CH_4 and (b) H_2 yields produced in the presence of all the fabricated photocatalysts. (c) Comparison of the photocatalytic CO, CH_4, and H_2 generation rates over the fabricated catalysts upon 5 h of simulated-solar-light illumination.

Fig. 9. (a) The amount of CH_4 production over the NLC-10 hybrid catalyst for prolonged CO_2 photoreduction reaction. (b) Reusability studies of CH_4 production over NLC-10 hybrid catalyst.

Fig. 10. (a) CO_2 adsorption isotherms and (b) steady-state PL patterns for CN, NCD/CN, LDH/CN, and all the NCD/LDH/CN hybrid catalysts. (c) Time-resolved PL patterns of CN, NCD/CN, LDH/CN, and NLC-10 samples. (d) Photocurrent responses of CN, NCD/CN, LDH/CN, and all the NCD/LDH/CN hybrid catalysts.

Fig. 11. Schematic illustration of the proposed mechanism for CO_2 photoreduction in the NCD/LDH/CN hybrid photocatalyst.

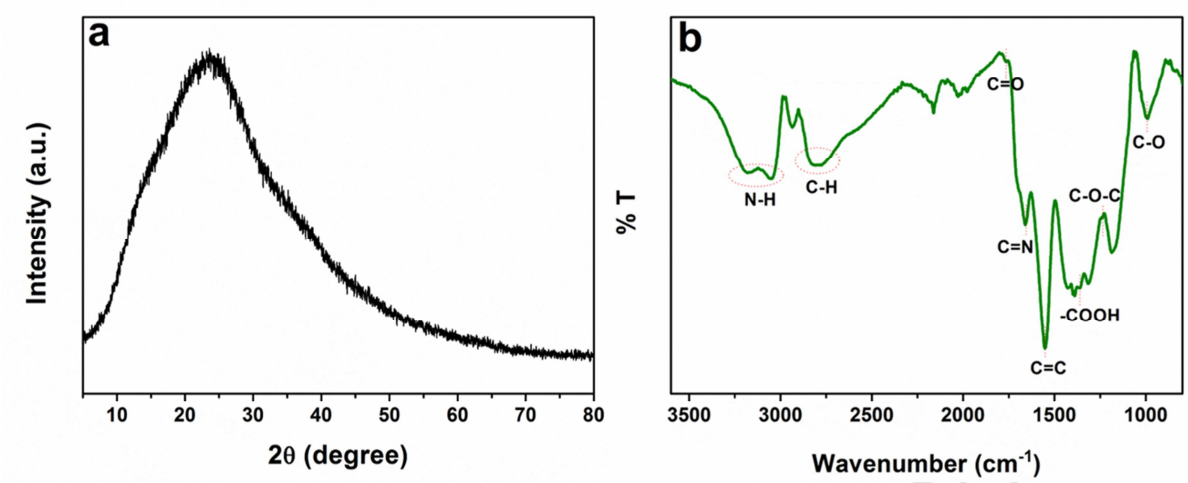

Fig. 1. (a) XRD and (b) FTIR patterns of the fabricated NCDs.

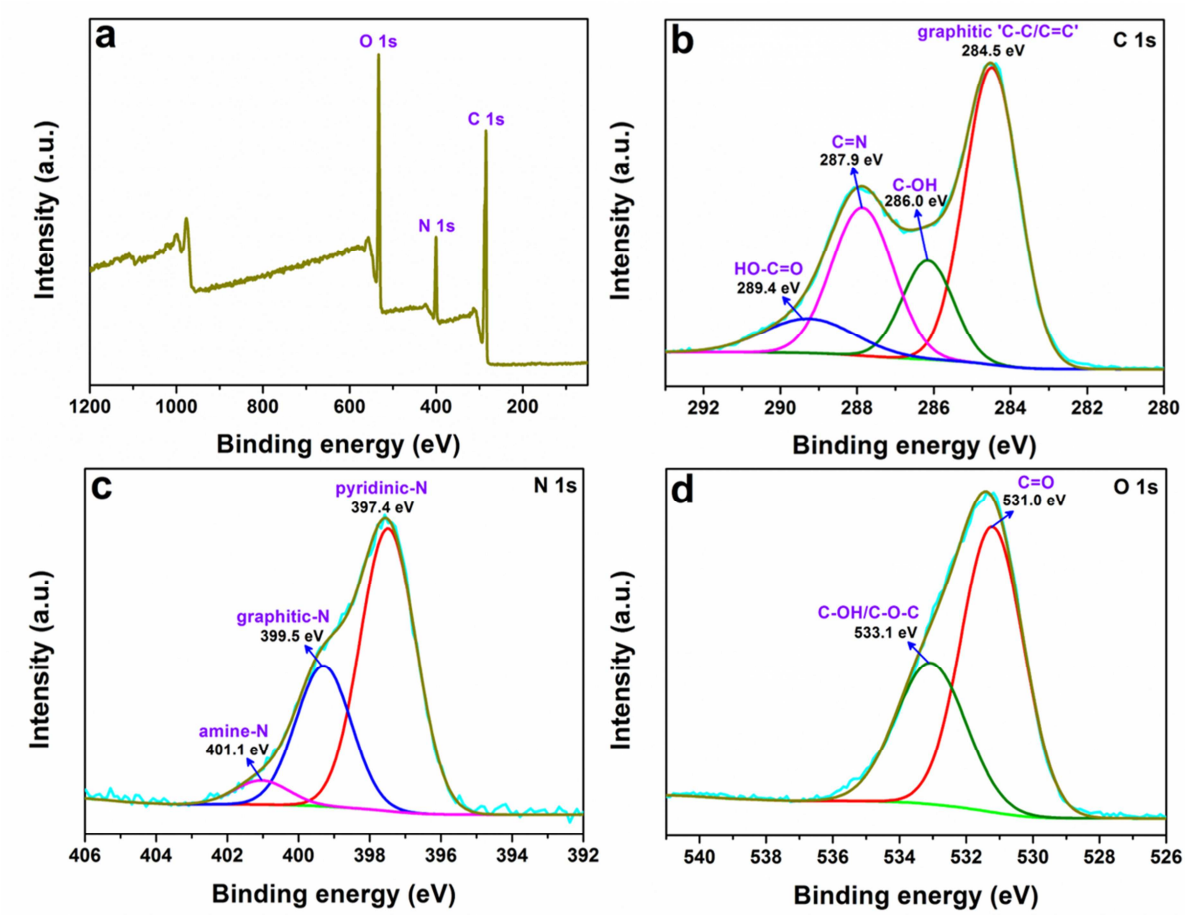

Fig. 2. XPS spectra of the NCDs. (a) Survey spectrum, (b) C 1s, (c) N 1s, and (d) O 1s.

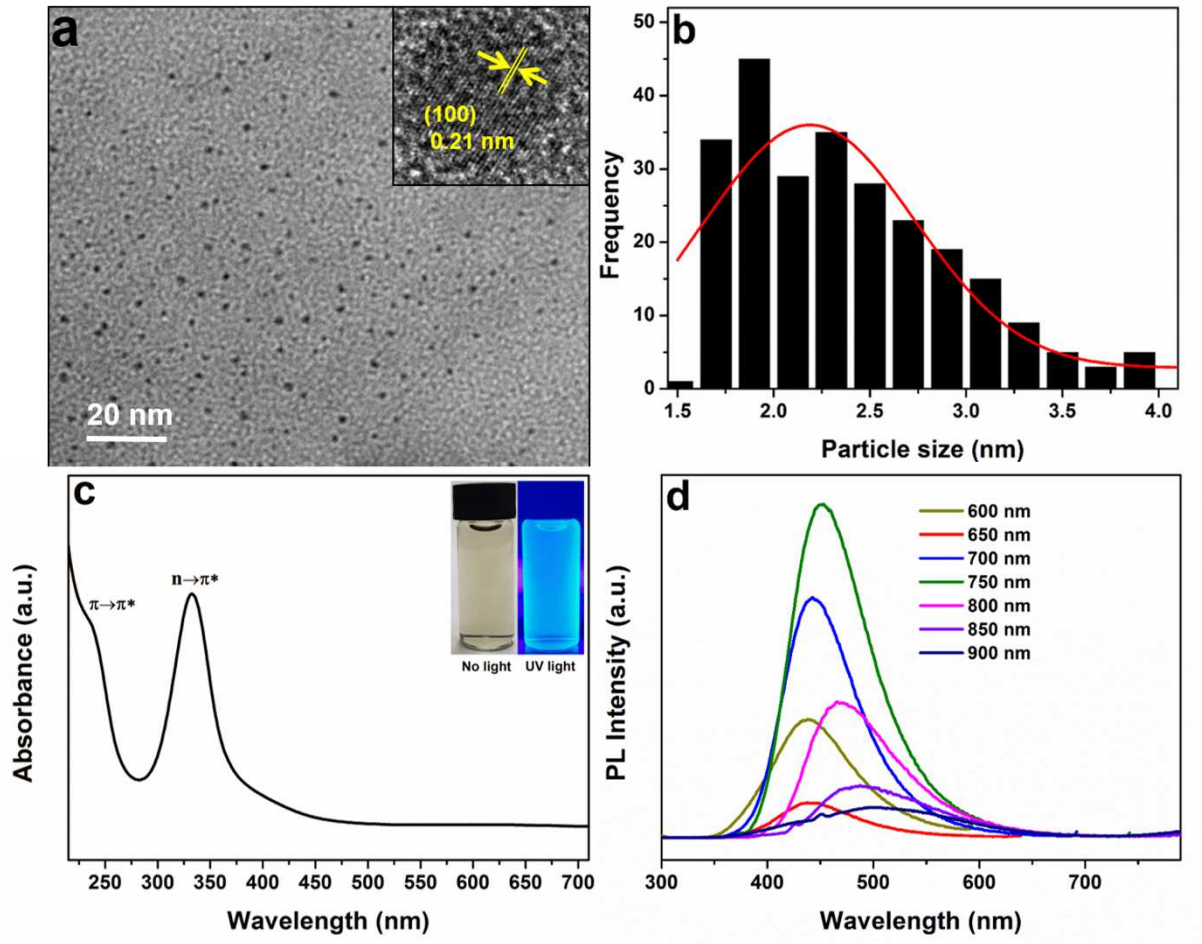

Fig. 3. (a) TEM image of the NCDs (inset is the HRTEM image) and (b) the corresponding particle size distribution histogram. (c) UV–vis absorption spectrum and (d) up-converted PL spectra of the NCDs.

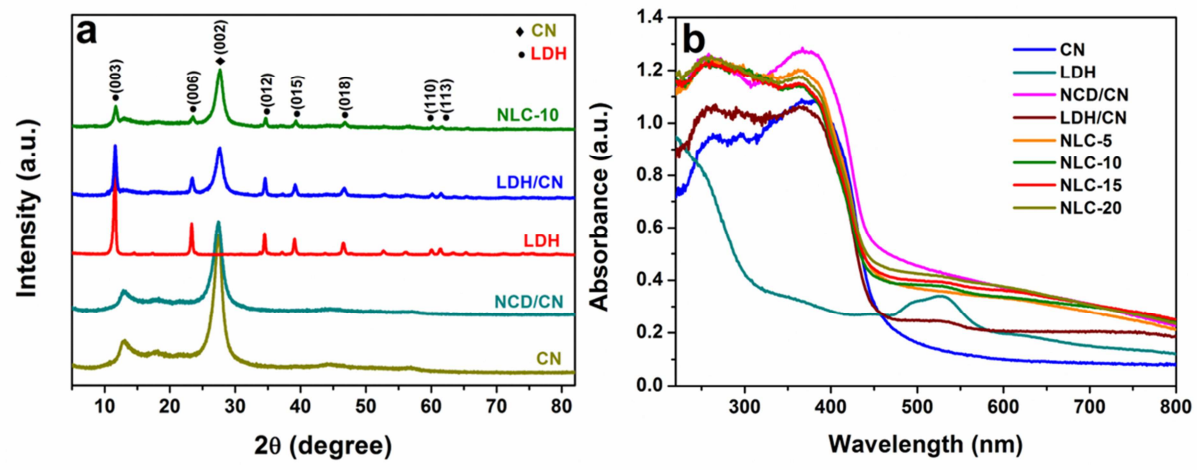

Fig. 4. (a) XRD and (b) DRS patterns of the prepared LDH, CN, NCD/CN, LDH/CN and NCD/LDH/CN hybrid samples.

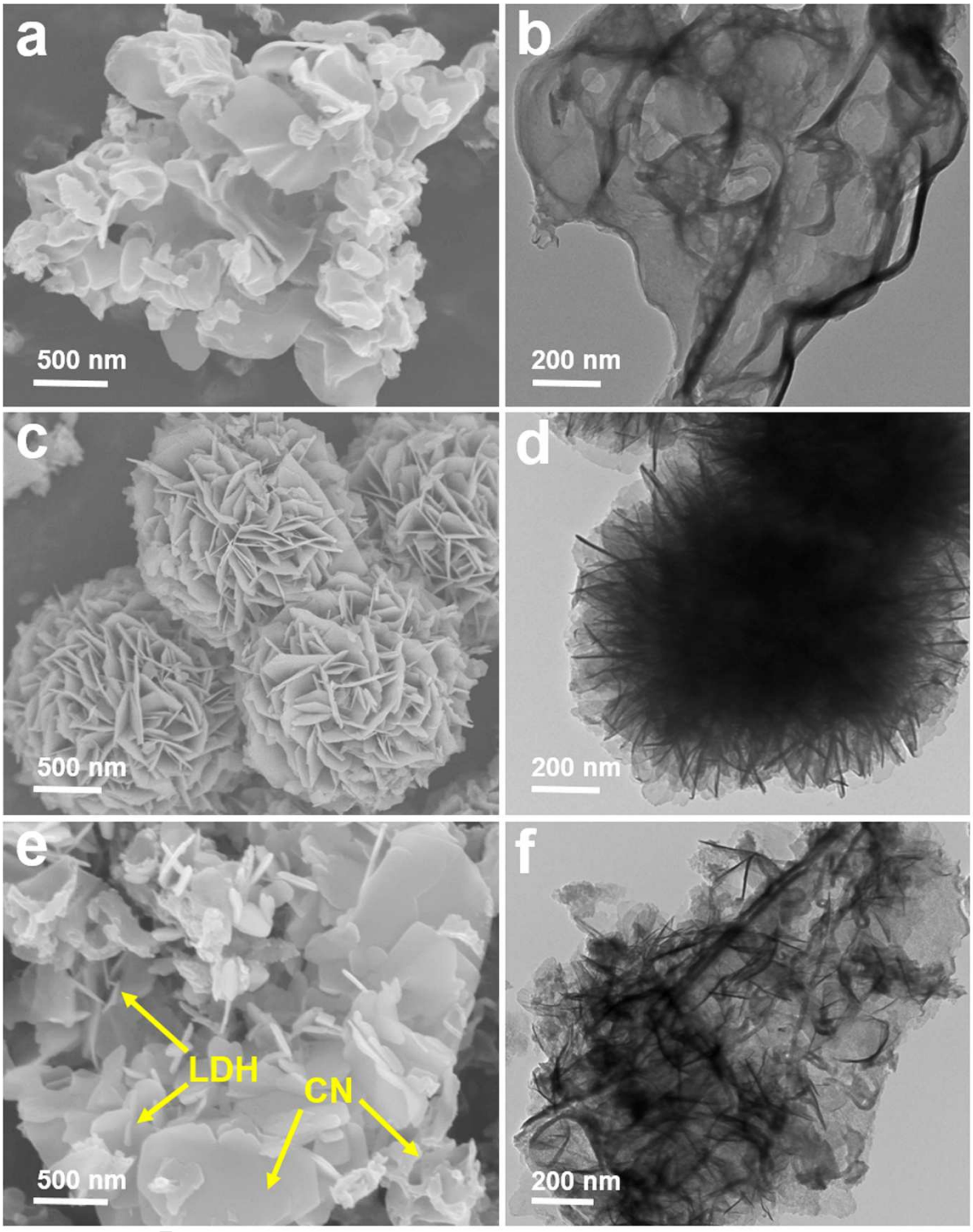

Fig. 5. (a, c, e) SEM and (b, d, f) TEM images of CN, LDH, and the NLC-10 catalysts, respectively.

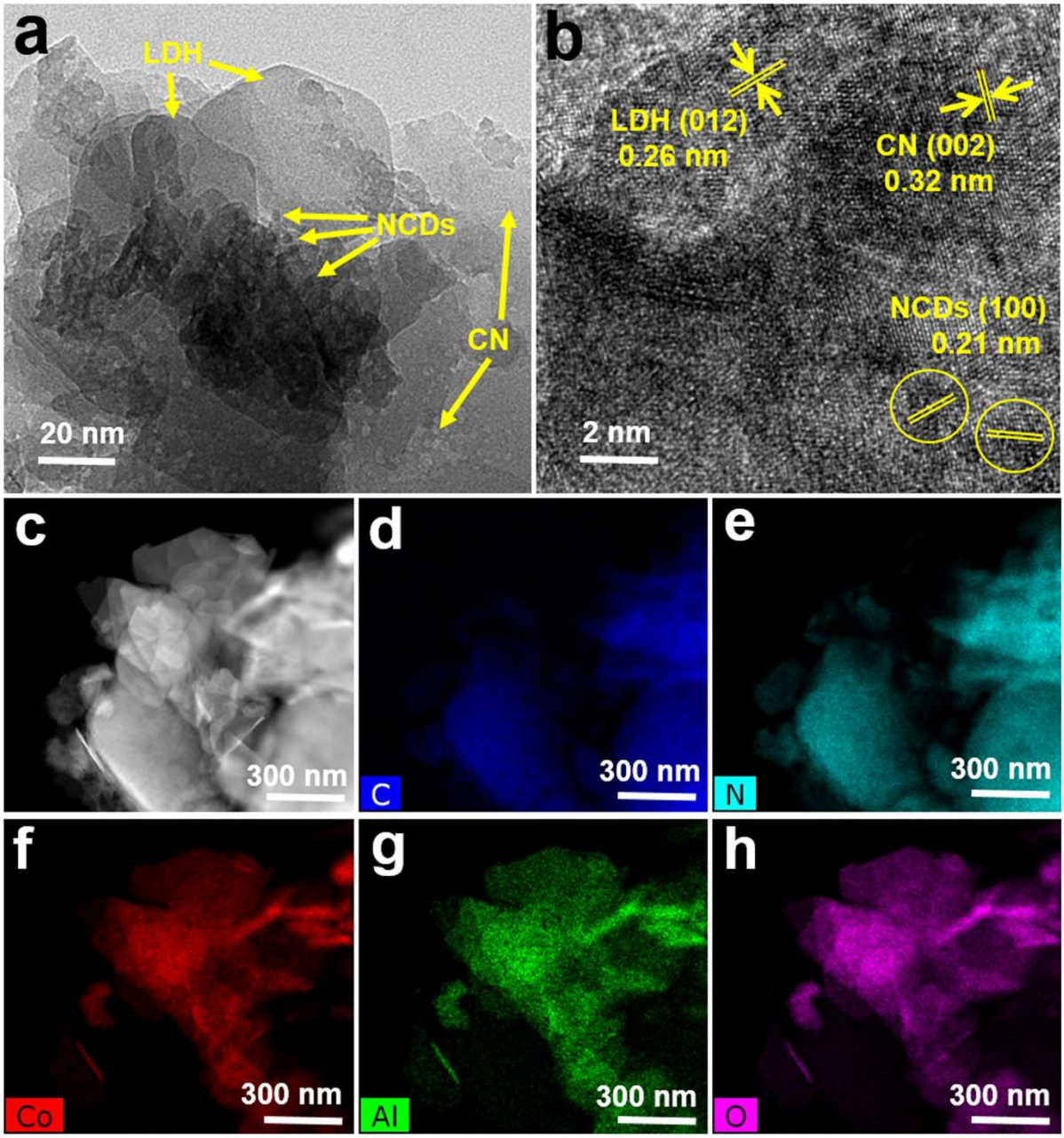

Fig. 6. High-resolution TEM images (a, b) of the NLC-10 hybrid photocatalyst. (c to h) EDS elemental mappings of constituent elements in the NLC-10 hybrid.

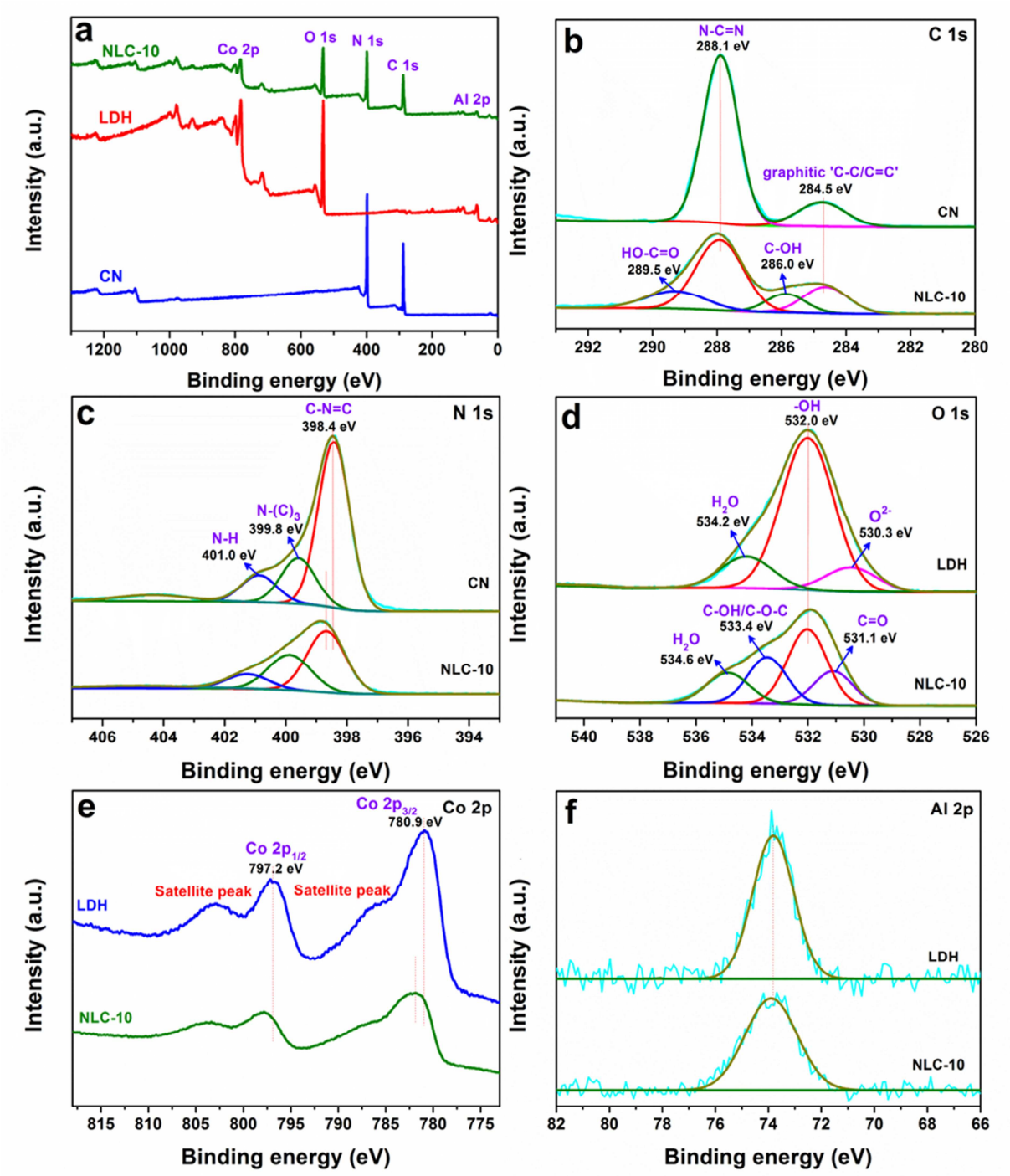

Fig. 7. XPS spectra of CN, LDH, and NLC-10 samples. (a) Survey spectra, (b) C 1s, (c) N 1s, (d) O 1s, (e) Co 2p, and (f) Al 2p.

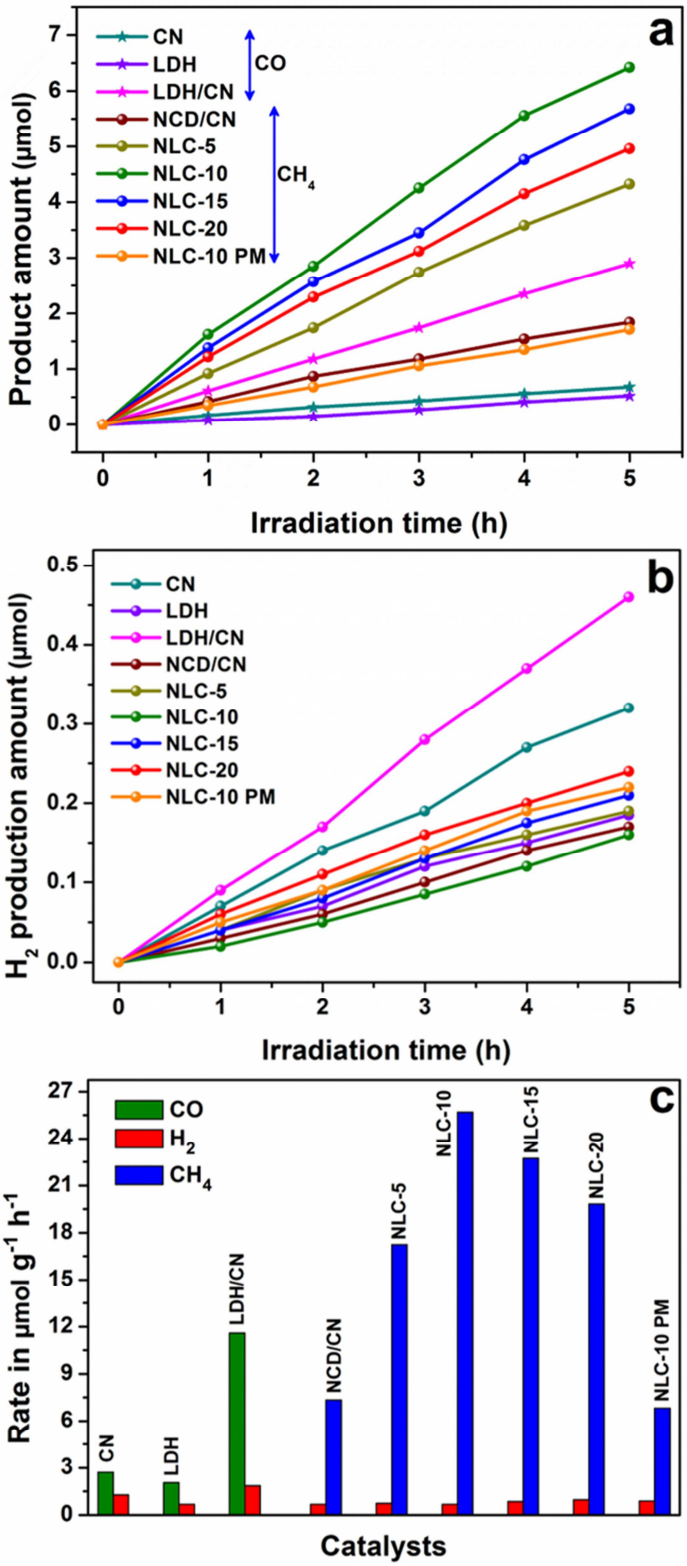

Fig. 8. Time-dependent (a) CO & CH_4 and (b) H_2 yields produced in the presence of all the fabricated photocatalysts. (c) Comparison of the photocatalytic CO, CH_4, and H_2 generation rates over the fabricated catalysts upon 5 h of simulated-solar-light illumination.

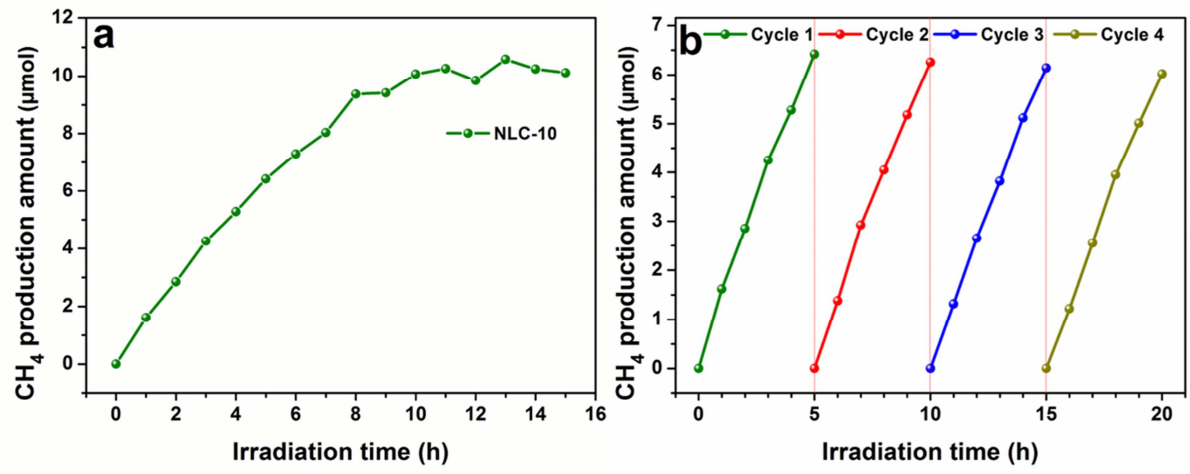

Fig. 9. (a) The amount of CH_4 production over the NLC-10 hybrid catalyst for prolonged CO_2 photoreduction reaction. (b) Reusability studies of CH_4 production over NLC-10 hybrid catalyst.

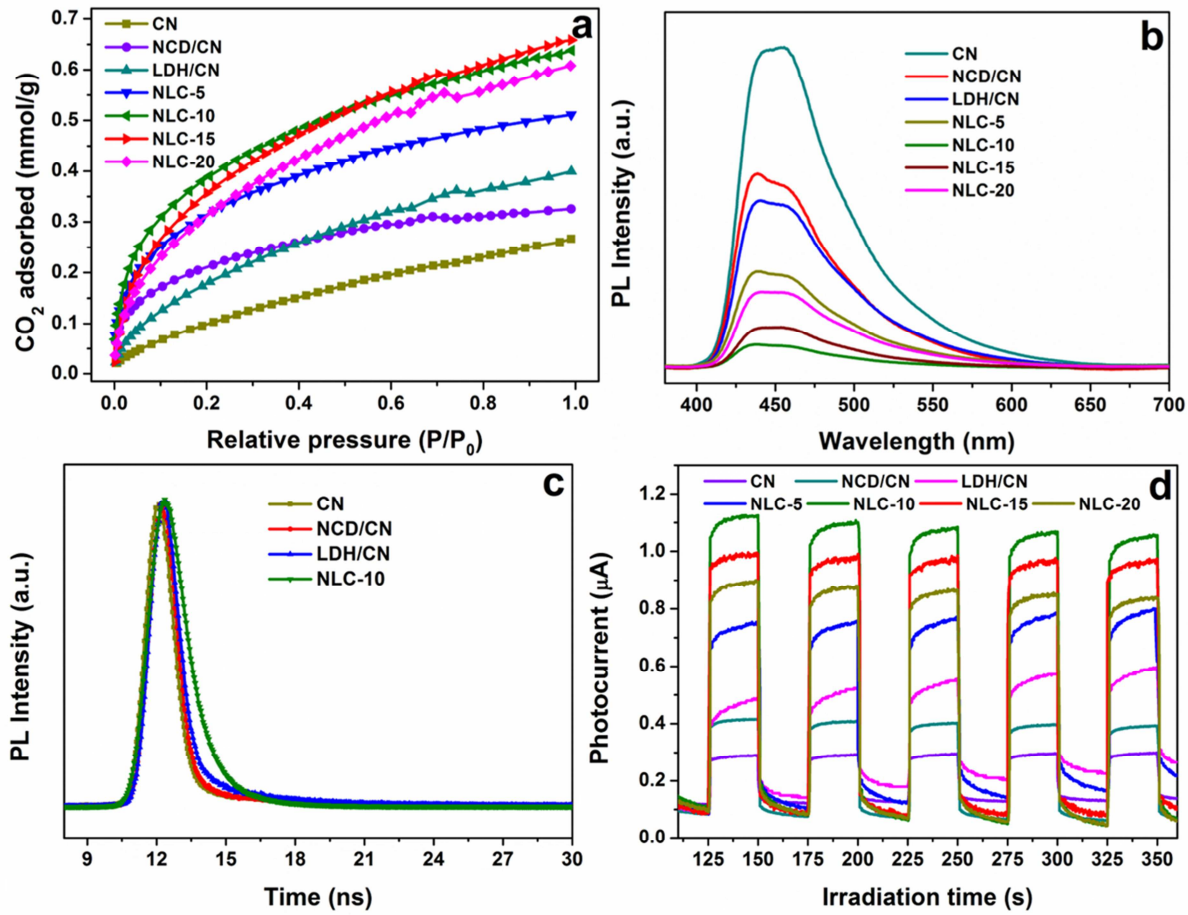

Fig. 10. (a) CO_2 adsorption isotherms and (b) steady-state PL patterns for CN, NCD/CN, LDH/CN, and all the NCD/LDH/CN hybrid catalysts. (c) Time-resolved PL patterns of CN, NCD/CN, LDH/CN, and NLC-10 samples. (d) Photocurrent responses of CN, NCD/CN, LDH/CN, and all the NCD/LDH/CN hybrid catalysts.

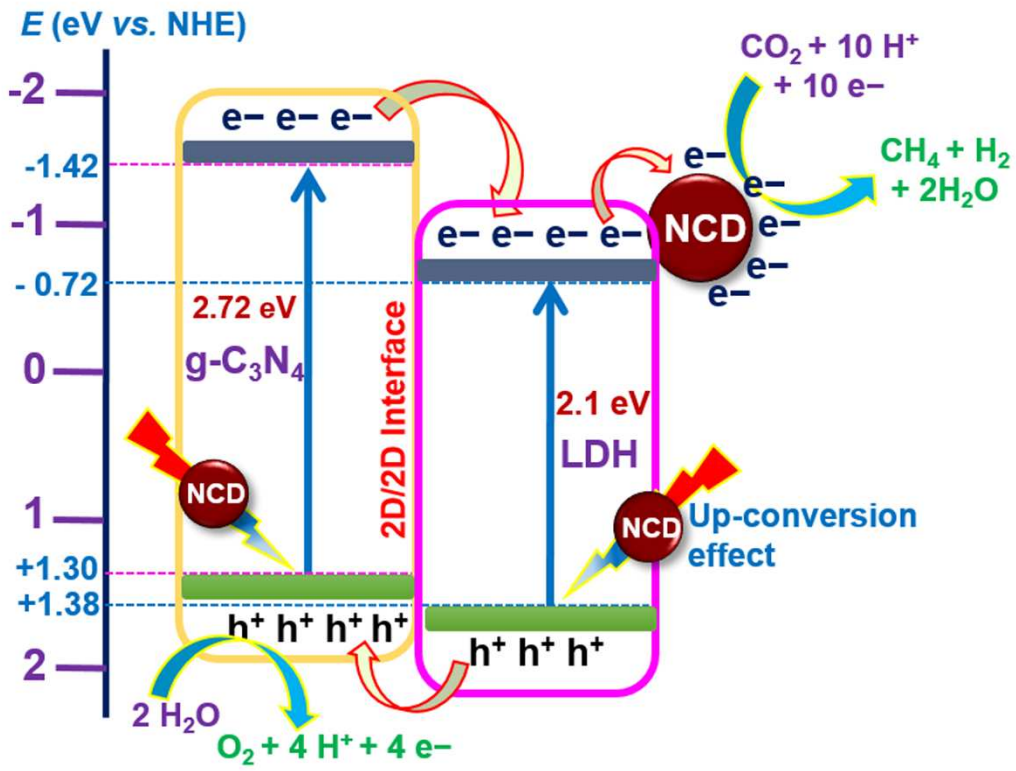

Fig. 11. Schematic illustration of the proposed mechanism for CO_2 photoreduction in the NCD/LDH/CN hybrid photocatalyst.

Highlights

- N-doped C dot/CoAl-LDH/g-C_3N_4 hybrid heterojunction was fabricated for the first time
- Hybrid heterojunction displayed exceptional CO_2 reduction performance to generate CH_4
- Rapid charge transfer owing to intimate interfacial contact contributed to high activity
- Hybrid catalyst displayed high stability and durability during consecutive test cycles
- NCDs played multiple roles for the efficient and selective production of CH_4 from CO_2 reduction